



Hexamethonium bromide-assisted synthesis of CoMo/graphene catalysts for selective hydrodesulfurization

Jundong Xu, Yunfeng Guo, Tingting Huang, Yu Fan*

State Key Laboratory of Heavy Oil Processing, China University of Petroleum, Beijing 102249, PR China



ARTICLE INFO

Keywords:
CoMo/Graphene
Selective hydrodesulfurization
Morphology
CoMoS
Hexamethonium bromide

ABSTRACT

A series of CoMo/graphene selective hydrodesulfurization (HDS) catalysts were prepared using the hexamethonium bromide-assisted hydrothermal method, and the influences of the hexamethonium bromide/Mo molar ratio and the CoMoS/MoS₂ ratio on the HDS activity and selectivity were investigated. The results show that the k_{HDS} value ($2.76 \times 10^{-7} \text{ mol g}^{-1} \text{ s}^{-1}$) of thiophene and the HDS selectivity factor (13.6) over the as-prepared catalysts were 1.3 times and 1.6 times greater than those over the CoMo/graphene prepared using the conventional impregnation method. The higher HDS activity and selectivity of the as-prepared catalysts result from the higher dispersion of Mo species and the higher CoMoS/MoS₂ ratio compared to the CoMo/graphene prepared by impregnation. Among all the catalysts, the catalyst with a hexamethonium bromide/Mo molar ratio of 6.0 presents the highest HDS selectivity due to its highest ratio of edge to corner Co atoms in CoMoS with a superior CoMoS/MoS₂ ratio. The present investigation provides a route for developing highly selective HDS catalysts using graphene as support by adjusting the hexamethonium bromide/Mo ratio to finely tune the morphology of the active phases.

1. Introduction

Restrictions on the sulfur content of gasoline are becoming stricter due to increasingly stringent environmental legislation to control exhaust gas (SO_x) from vehicles [1,2]. These gases pollute the environment and lead to human health problems; moreover, SO_x gases reduce the efficiency of the plant units and cause a severe corrosion of the reactors [3]. Most sulfur (> 90%) in commercial gasoline results from fluid catalytic cracking (FCC) gasoline; therefore, the key to reducing sulfur in commercial gasoline lies in the desulfurization of this stream [4,5]. In addition, FCC gasoline also contains a large number of olefins, which are significant for maintaining the octane number of commercial gasoline. However, olefins with high octane numbers are easily hydrogenated during the hydrodesulfurization (HDS) reaction because of its high reactivity [6–8]. Therefore, developing a highly selective HDS process with minimal olefin saturation to preserve the octane number and maximal desulfurization to meet the stringent legislation on sulfur content is desired [9]. The preparation of highly selective HDS catalysts is an effective route to improve selective HDS performance.

Transition metal sulfide catalysts have been widely used in HDS [5,10]. Among these catalysts, molybdenum-based sulfide catalysts supported on alumina are often used in HDS [11,12]. However, this type of catalyst has both high hydrogenation (HYD) and HDS activities,

resulting in the saturation of most olefins and great loss in octane number of the product [13–15]. Extensive studies have been performed to enhance the HDS selectivity of this catalyst by incorporating potassium [16,17], adding chelation agents [18,19] and changing the support [20,21]. Nikulshin et al. and Fan et al. [16,22] found that the incorporation of potassium led to an increase in the average length of MoS₂ slabs and partial poisoning of active sites, which resulted in a decrease in catalyst activity. The sensitivity of olefin HYD to potassium is much higher than thiophene HDS, thus improving the HDS selectivity of the potassium-modified catalyst. Using different kinds of chelation agents, Nikulshin et al. [19] investigated the effects of the content and edge-to-corner ratio of CoMoS phases on the HDS selectivity; they proposed that a high content and edge-to-corner ratio of CoMoS phases promoted the HDS reaction but had little effect on olefin HYD. Li et al. [20] investigated several CoMo catalysts with different supports; they found that the average length of MoS₂ slabs related to the HDS selectivity can be adjusted through the different type of supports.

Recently, carbon materials have received attention as a support for catalysts because of their high surface area, high adsorptive capacity and low cost. Carbon materials can be synthesized from a variety of sources such as wood, charcoal, rubber tires, animal bones, peat, and biochar et al. [23,24]. Moreover, it has been found that carbon-supported CoMo catalysts present more activity than alumina-supported

* Corresponding author.

E-mail address: fanyu@cup.edu.cn (Y. Fan).

catalysts for thiophene HDS, and the high activity of these catalysts is believed to result from the weak interaction between the CoMoS phase and the support [25,26]. However, most of the surface area of traditional activated carbon is accounted for by micropores; after loading the metal, the micropores are easily blocked, which is a disadvantage for the diffusion of reactants or products [26]. Graphene, as a new style of carbon material, has the advantages of using carbon as a support without structural limitations [27,28]. Unfortunately, the dispersion of graphene is poor in aqueous solution [29], but graphene oxide (GO) with abundant epoxide and hydroxyl groups on the basal planes and abundant carboxylic groups at the edges has good dispersion in aqueous solution [30]. These functional groups on GO can be easily assembled with inorganic species [31]. As a consequence, GO has been widely used in composite materials, solar cells, batteries and catalysts [32–35]. However, the application of CoMo/graphene in selective HDS has not been reported.

Herein, we propose a novel strategy for preparing a finely adjusted morphology of (Co)MoS₂ on GO via a hexamethonium-assisted hydrothermal method. In this method, the hexamethonium bonds to the negatively charged surface of GO through an electrostatic interaction and converts the surface of GO into the positively charged surface, which overcomes the charge incompatibility between MoS₄²⁻ and the negatively charged GO. With obtaining a different number of positive charges on the GO surface by adjusting the content of added hexamethonium, the morphology of active (Co)MoS₂ is finely tuned. The as-prepared catalysts exhibited much higher HDS activity and selectivity compared to the GO-supported (Co)MoS₂ catalyst that was prepared using the impregnation method.

2. Experimental section

2.1. Materials

GO was purchased from the Suzhou Tanfeng Graphene Technology Company Ltd. Hexamethonium bromide ((CH₃)₃N(CH₂)₆N(CH₃)₃Br₂, 98%, denoted HMB) was obtained from the Shanghai TCI Development Company Ltd. The elemental compositions of the GO were C: 54.93 wt. %, H: 2.88 wt. %, O: 41.24 wt. %, N: 0.12 wt. % and S: 0.83 wt. %. Ammonium tetrathiomolybdate ((NH₄)₂MoS₄, 99%, denoted ATTM) and thiophene (C₄H₈S, 99%) were purchased from Beijing J & K Scientific Ltd. Cobalt nitrate hexahydrate (Co(NO₃)₂·6H₂O, 99%), cyclohexane (C₆H₁₂, 99%), carbon disulfide (CS₂, 99%), n-heptane (C₇H₁₆, 99%) and 1-hexene (C₆H₁₂, 99%) were obtained from the Beijing Chemical Reagent Company. The above reagents were used without further purification.

2.2. Preparation of catalysts

A series of MoS₂/GO catalysts were prepared using an HMB-assisted hydrothermal method. In a typical synthesis procedure, 0.052 g HMB was added to 65 mL deionized water containing GO (0.065 g), and the suspension was stirred at 40 °C for 12 h. Afterward, 0.018 g ATTM were dissolved in deionized water (15 mL) with ultrasonication for 30 min and were dropped into the above suspension. The resultant suspension was transferred into an autoclave, and the autoclave was heated at 120 °C for 12 h while rotated. After cooling naturally, the product was collected by centrifugation and was washed with deionized water. Finally, the collected product was dried in the vacuum oven at 60 °C for 12 h and was calcined at 450 °C for 4 h in nitrogen. By adjusting the added amount of HMB, catalysts with different HMB/Mo ratios were prepared. The obtained catalysts are designated MoS₂/GO-HMBx, where x is the molar ratio of HMB/Mo (x = 2, 4, 6, 8).

The MoS₂/GO-IM sample was prepared using incipient wetness impregnation. 0.108 g of ATTM was dissolved in a mixed solution of ethanolamine and deionized water (1:1, v/v); then, the solution was added to GO (0.600 g) dropwise. After impregnation, the catalyst was

Table 1
Compositions of the prepared catalysts after sulfidation.

Catalyst	MoS ₂ (wt. %)	Co/(Co + Mo) molar ratio	Mo (wt. %)	Co (wt. %)
s-CoMo/G-IM	13.1	0.31	7.85	2.17
s-CoMo/G-HMB2	13.1	0.30	7.85	2.07
s-CoMo/G-HMB4	13.0	0.31	7.79	2.15
s-CoMo/G-HMB6	13.1	0.30	7.85	2.07
s-CoMo/G-HMB8	13.0	0.30	7.79	2.05

dried and calcined according to the same process that was used for MoS₂/GO-HMBx.

The loading of cobalt species on the above MoS₂/GO catalysts was conducted by impregnating MoS₂/GO-HMBx and MoS₂/GO-IM with cobalt nitrate (Co(NO₃)₂·6H₂O, 98 wt.%) as the cobalt precursor. Following impregnation, the obtained products were dried in a vacuum oven at 60 °C for 12 h and were calcined at 450 °C for 4 h in nitrogen. Finally, the samples were sulfided with carbon disulfide (3.0 wt.%) in n-heptane at 2 MPa and 360 °C for 4 h to produce the sulfided CoMo/graphene catalysts, denoted as s-CoMo/G-HMBx and s-CoMo/G-IM. The compositions of these catalysts determined by inductively coupled plasma optical emission spectroscopy (ICP-OES) are listed in Table 1.

2.3. Characterizations

The compositions of the samples were analyzed by ICP-OES on a Perkin Elmer apparatus. Elements C, H, O, N and S of GO were analyzed by a Perkin Elmer instrument combined with 2400 II CHON/S element analyzer. The zeta potentials of the samples were measured on a Zetasizer Nano ZS instrument.

Fourier transform infrared (FT-IR) spectra were observed using a VERTEX 80v instrument (Germany) with a high-sensitivity detector MCT at a 4 cm⁻¹ resolution.

Raman experiments were conducted on a LabRAM Aramis Raman spectrometer with a laser excitation wavelength of 532 nm.

X-ray diffraction (XRD) patterns were obtained on a Bruker D8 Advance instrument with Cu K α radiation ($\lambda = 1.54 \text{ \AA}$), 40 kV, 30 mA, a scanning speed 4°/min, and ranging from 5 to 80°.

N₂ adsorption-desorption experiments of the support GO and the catalysts were performed on a Micromeritics ASAP 2420 instrument. The samples were pretreated at 150 °C under a vacuum of 10⁻³ Pa for 24 h prior to the experiments, and subsequently transferred to the analysis station for adsorption-desorption at -196 °C.

The H₂ temperature-programmed reduction (H₂-TPR) analyses of the samples were measured on a home-built device. Each catalyst (0.1 g) was pretreated at 150 °C for 1 h in an Ar stream and then the catalyst was cooled to 60 °C. Then, the catalyst was heated to 800 °C at a rate of 10 °C/min in a 10% H₂/N₂ flow. The H₂ consumption during the reduction process was determined using a TCD detector.

The morphologies of the metal species supported on graphene were performed on an FEI Tecnai G2 F30 high-resolution transmission electron microscope (HRTEM) operating at 300 kV and equipped with an energy-dispersive X-ray spectrometer (EDX). The samples were prepared by adding a drop of the ultrasonicated catalyst suspension in ethanol on a copper micro grid. Twenty representative pictures were acquired for each catalyst, including 300–500 slabs acquired from different regions of each catalyst. The average stacking number (\bar{N}) and slab length (\bar{L}) were expressed by the following equations [18,36,37]:

$$\bar{N} = \frac{\sum_{i=1}^n x_i N_i}{\sum_{i=1}^n x_i} \quad \text{and} \quad \bar{L} = \frac{\sum_{i=1}^n x_i L_i}{\sum_{i=1}^n x_i} \quad (1)$$

where N_i and L_i are the layer number and length of MoS₂ slabs in each stack, respectively, and x_i is the number of MoS₂ slabs with N_i layers of length L_i .

MoS₂ dispersion (D) was calculated using the following equation

[18,38]:

$$D = \frac{Mo_e + Mo_c}{Mo_T} = \frac{\sum_{i=1}^t (6n_i - 6)}{\sum_{i=1}^t (3n_i^2 - 3n_i + 1)} \quad (2)$$

where n_i is the number of Mo atoms along one edge of a MoS_2 slab, determined by its length ($L = 3.2(2n_i - 1) \text{ \AA}$); t is the total number of slabs; and Mo_T , Mo_e and Mo_c are the total number of Mo atoms and the number of Mo atoms at the edge and corner sites, respectively.

The edge-to-corner ratio of a MoS_2 slab (f_e/f_c)_{Mo} was expressed by the following equation [38]:

$$(f_e/f_c)_{Mo} = \frac{Mo_e}{Mo_c} = \frac{10 \times \bar{L}/3.2 - 3}{2} \quad (3)$$

X-ray photoelectron spectroscopy (XPS) experiments of the catalysts were conducted on a Thermo Fisher K-Alpha electron spectrometer equipped with an Al K α monochromatic source with an energy resolution of 0.4 eV. Before measurement, the catalyst was sealed in cyclohexane to avoid oxidation. The C 1s peak at 284.6 eV was used as a reference in the determination of binding energies. The Co 2p and Mo 3d spectra were decomposed using the software of XPSPEAK version 4.1, applying a Shirley-Linear background subtraction and mixed Gaussian-Lorentzian function [39].

The analysis of the XPS spectra allowed quantification of the absolute amount of each species [40]:

$$C(i) = \frac{A_i / S_i}{\sum_{i=1}^n A_i / S_i} \times 100 \quad (4)$$

where $C(i)$ is percentage of species i , A_i is the measured area of species i , and S_i is the sensitivity factor of the atom related to species i offered by the constructor.

The calculation of the respective contribution of each peak area helps to understand the relative proportion of each species. Accordingly, the relative concentrations of each species (MoO_3 (Mo^{6+}), MoS_xO_y (Mo^{5+}), MoS_2 (Mo^{4+}), CoO_x , CoMoS and CoS_x) were determined for each catalyst. The relative content of CoMoS was calculated by the following equation [41]:

$$\% \text{CoMoS} = \frac{A_{\text{CoMoS}}}{A_{\text{CoMoS}} + A_{\text{CoS}_x} + A_{\text{CoO}_x}} \times 100 \quad (5)$$

where A_{CoMoS} , A_{CoS_x} and A_{CoO_x} represent the experimental XPS areas of CoMoS , CoS_x and CoO_x species, respectively.

The effective concentration of the CoMoS phases was expressed by the following equation [40]:

$$C_{\text{CoMoS}} = \% \text{CoMoS} \times C(\text{Co}) \quad (6)$$

where $C(\text{Co})$ is the effective concentration of Co obtained from XPS.

The CoMoS phases edge-to-corner ratio (f_e/f_c)_{CoMo} was expressed by the following equation [19]:

$$(f_e/f_c)_{\text{CoMo}} = (f_e/f_c)_{\text{Mo}} \times \frac{C_{\text{CoMoS}}/C_{\text{MoS}_2}}{D} \quad (7)$$

2.4. Catalyst assessment

The density of the used catalysts was about 0.35 g cm^{-3} , and their particle sizes were in the range of 20–40 meshes. A mixture of 1-hexene (30 wt.%) and thiophene (500 $\mu\text{g/g}$ S) in heptane was used as a model gasoline to test the catalytic performance of the series of catalysts in a continuous-flow tubular fixed-bed microreactor of internal diameter 8.0 mm and length 300 mm. The catalyst of 20–40 meshes was mixed with the same volume and size of quartz granules. The catalytic performance of the catalyst was tested under the following conditions: H_2 /model gasoline ratio of 300 (v/v), 1.5 MPa, 280 °C and liquid hourly space velocity (LHSV) 4 h^{-1} . After the stable state was reached, the liquid product was collected. The total sulfur content of the liquid product was measured on an Analytik Jena Multi EA 5000 apparatus

and the international standard of ASTM D5453 was used. The hydrocarbon composition of the liquid product was measured on an SP3420 gas chromatograph equipped with an HP-PONA (50 m \times 0.2 mm) capillary column and a flame ionization detector (FID).

The desulfurization ratio (X_S) and the olefin conversion through hydrogenation (X_O) were determined by the following equations:

$$X_S = \frac{C_S^0 - C_S}{C_S^0} \times 100 \quad \text{and} \quad X_O = \frac{C_O^0 - C_O}{C_O^0} \times 100 \quad (10)$$

where C_S and C_S^0 are the total sulfur mass fractions in the products and feedstock, respectively, and C_O and C_O^0 are the olefin content in the products and feedstock, respectively.

The ratio of the thiophene HDS activity to the olefin HYD activity is defined as the HDS selectivity factor (SF) and is calculated by the following equation [7]:

$$\text{SF} = \frac{\ln(C_S/C_S^0)}{\ln(C_O/C_O^0)} \quad (11)$$

The 1-hexene HYD and thiophene HDS were assumed as a pseudo-first order reaction, and the reaction rate constants were calculated by the following equation [42]:

$$k_{\text{HYD}} = \frac{F_O}{m} \ln\left(\frac{1}{1 - X_O}\right) \quad \text{and} \quad k_{\text{HDS}} = \frac{F_S}{m} \ln\left(\frac{1}{1 - X_S}\right) \quad (12)$$

where k_{HYD} and k_{HDS} are the reaction rate constants of 1-hexene HYD and thiophene HDS in $\text{mol} \cdot \text{g}^{-1} \cdot \text{s}^{-1}$, respectively, F_O and F_S are the molar feed rate of 1-hexene and thiophene in $\text{mol} \cdot \text{s}^{-1}$, respectively, m is the catalyst mass in grams, and X_O and X_S are the olefin conversion through hydrogenation and desulfurization ratio, respectively.

3. Results and discussion

3.1. XRD and N_2 adsorption-desorption

Fig. 1 shows the XRD patterns of GO, s-CoMo/G-IM and s-CoMo/G-HMBx prepared according to the HMB-assisted hydrothermal method. Compared to GO, the sulfided catalysts have not typical GO (001) peak at $2\theta = 11.1^\circ$, suggesting that GO was reduced into graphene. In the XRD patterns of the sulfided catalysts, there is a new peak at $2\theta = 26.0^\circ$, which is assigned to the characteristic peak of the (002) plane of graphene. For s-CoMo/G-IM, except for the peak attributed to graphene, there are peaks at $2\theta = 14.2^\circ$ and 32.9° , which are attributed to the (002) and (100) planes of the 2H- MoS_2 (hexagonal structure) (JCPDS card no. 37-1492), respectively. The MoS_2 (002) peak at $2\theta = 14.2^\circ$ indicates a multilayered MoS_2 structure over s-CoMo/G-IM [43]. In contrast, no multilayered MoS_2 peaks at $2\theta = 14.2^\circ$ are detected in the XRD patterns of s-CoMo/G-HMBx, suggesting that the MoS_2 nanoparticles on these catalysts are well-dispersed on graphene. No characteristic peaks of cobalt species were observed in the XRD patterns because of low cobalt loading on all the catalysts.

The N_2 adsorption-desorption isotherms of GO, s-CoMo/G-IM and s-CoMo/G-HMBx indicate that all the isotherms are type IV (Fig. S1) [44]. The hysteresis loops at relative pressures (P/P_0) greater than 0.45 are type H4, which are associated with aggregation of plate-like particles or slit-shaped pores [45]. Compared to the GO support, the surface area and the pore volume of CoMo/graphene decrease due to loading of the metal species (Table S1). The surface area and the pore volume of s-CoMo/G-IM are smaller than s-CoMo/G-HMBx (Table S1) because s-CoMo/G-IM has larger particles of Mo species that cause partial closing of the graphene pores. With an increasing HMB content in s-CoMo/G-HMBx, the surface area and the pore volume of s-CoMo/G-HMBx increase, indicating that the size of Mo species supported on graphene decreases with the increasing HMB content.

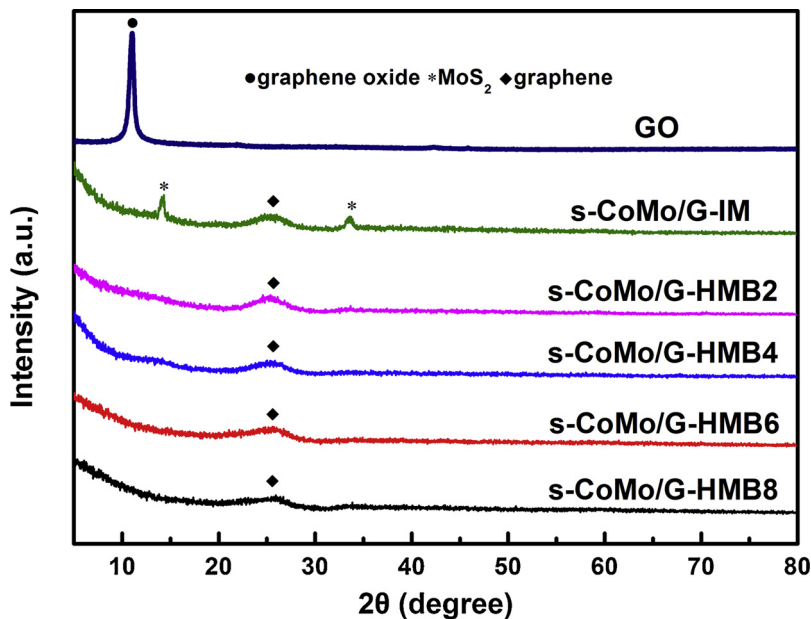


Fig. 1. XRD patterns of GO, s-CoMo/G-IM and s-CoMo/G-HMBx.

3.2. Raman spectroscopy

Raman spectroscopy can provide structural information about the stacking of MoS₂ supported on graphene. Raman spectra for MoS₂ show four first-order Raman-active modes: A_{1g} (408 cm⁻¹), E_{2g}¹ (383 cm⁻¹), E_{1g} (286 cm⁻¹) and E_{2g}² (32 cm⁻¹) [46]. For forbidden Raman back-scattering experiments, the E_{1g} is silent in the Raman spectra [47]. The E_{2g}² (associated with interlayer stacking of MoS₂) is difficult to observe because it is out of the detection range of a typical Raman spectrometer [47]. Generally, the A_{1g} vibration produces a blue shift, while the E_{2g}¹ vibration produces a red shift, and the distance between A_{1g} and E_{2g}¹ ($\Delta\omega = \nu(A_{1g}) - \nu(E_{2g}^1)$) increases with the increasing layer number of MoS₂ [47,48]. To obtain the stacking layer number of MoS₂, the graphene supported cobalt and molybdenum (CoMo/G) catalysts were characterized using a Raman spectrometer, the results of which are shown in Fig. 2. s-CoMo/G-IM displays two peaks at 407.0 and

382.2 cm⁻¹ that are attributed to A_{1g} and E_{2g}¹, respectively, and $\Delta\omega = 24.8$ cm⁻¹. s-CoMo/G-HMB2 displays two peaks at 405.8 cm⁻¹ (A_{1g}) and 382.7 cm⁻¹ (E_{2g}¹) ($\Delta\omega = 23.1$ cm⁻¹), s-CoMo/G-HMB4 displays two peaks at 405.0 cm⁻¹ (A_{1g}) and 383.1 cm⁻¹ (E_{2g}¹) ($\Delta\omega = 21.9$ cm⁻¹), s-CoMo/G-HMB6 displays two peaks at 404.3 cm⁻¹ (A_{1g}) and 383.5 cm⁻¹ (E_{2g}¹) ($\Delta\omega = 20.8$ cm⁻¹) and s-CoMo/G-HMB8 displays two peaks at 403.0 cm⁻¹ (A_{1g}) and 384.0 cm⁻¹ (E_{2g}¹) ($\Delta\omega = 19.0$ cm⁻¹). Compared to s-CoMo/G-IM, the A_{1g} peak of s-CoMo/G-HMBx has a red shift, whereas the E_{2g}¹ peak has a blue shift; the value of $\Delta\omega$ decreases, implying that the CoMo/G catalysts prepared using the HMB-assisted hydrothermal method has a lower stacking layer number of MoS₂ [48,49]. With the increasing HMB content in s-CoMo/G-HMBx, the value of $\Delta\omega$ decreases, indicating that the stacking layer number of MoS₂ in s-CoMo/G-HMBx decreases. Fig. 2 also shows two dominant peaks associated with graphene at 1600 cm⁻¹ (G-band) and 1360 cm⁻¹ (D-band). The G-band is assigned to the vibration of sp²

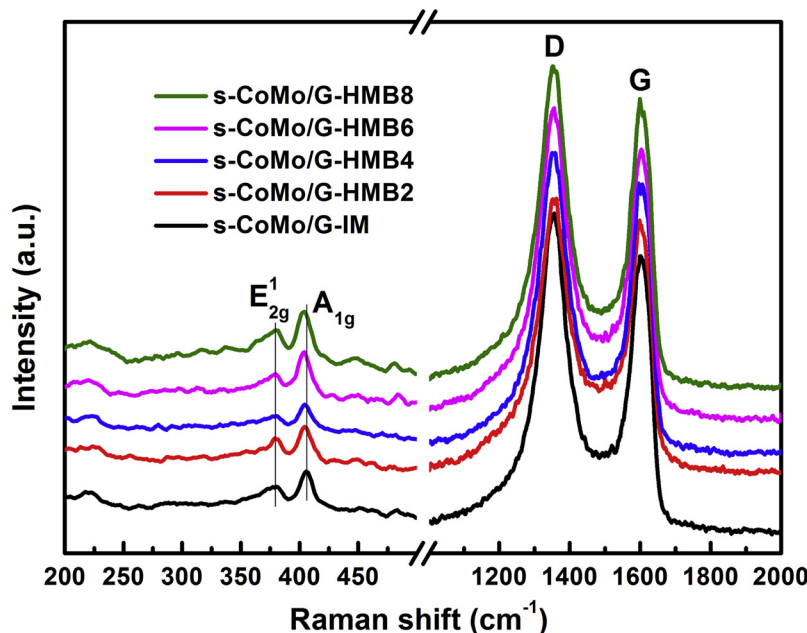


Fig. 2. Raman spectra of s-CoMo/G-IM and s-CoMo/G-HMBx.

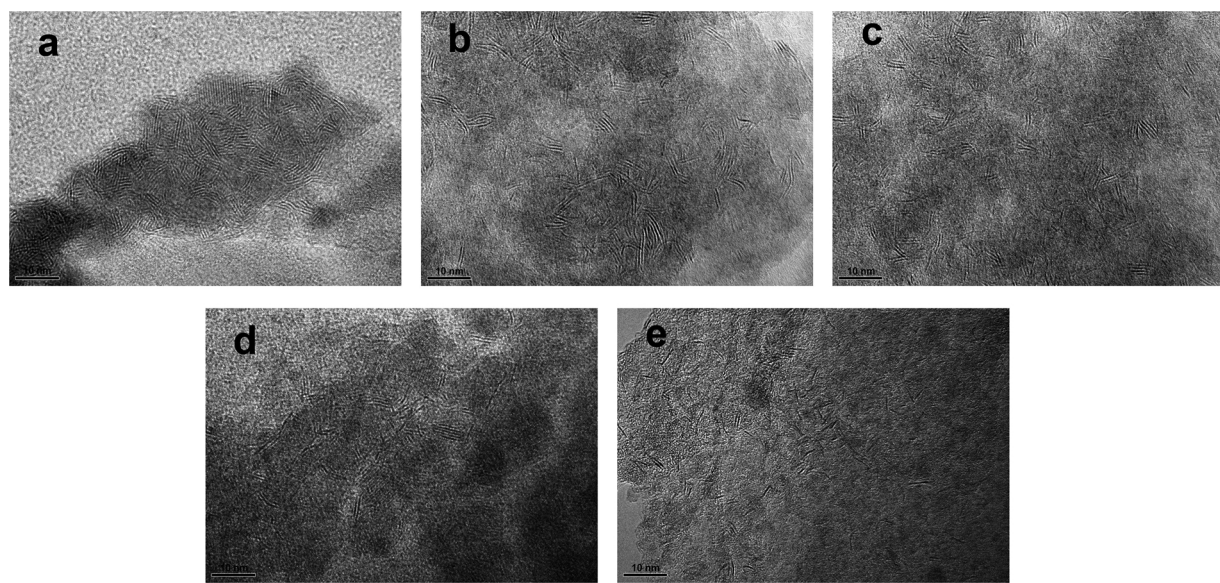


Fig. 3. HRTEM images of s-CoMo/G-IM (a), s-CoMo/G-HMB2 (b), s-CoMo/G-HMB4 (c), s-CoMo/G-HMB6 (d) and s-CoMo/G-HMB8 (e).

carbon atoms in a 2D hexagonal lattice, whereas the D-band represents edges, disorder and defects in the hexagonal graphitic layers [50]. The relative intensity ratio of I_D/I_G can be regarded as an indication of defects in carbon materials [51]. The calculated values of I_D/I_G for s-CoMo/G-IM and s-CoMo/G-HMBx are 1.18, 1.33, 1.40, 1.43 and 1.48, respectively. Compared to s-CoMo/G-IM, s-CoMo/G-HMBx has higher I_D/I_G values, indicating that s-CoMo/G-HMBx has more defects in the graphene support [50]. The abundant defects in s-CoMo/G-HMBx may result from the presence of amorphous carbon from the carbonization of HMB. Therefore, Raman spectroscopy demonstrates that with the increasing HMB content in s-CoMo/G-HMBx, the layer number of MoS₂ decreases and the defects associated with the graphene support increases.

3.3. HRTEM

The catalysts were characterized by HRTEM to acquire information regarding the distribution and morphology of MoS₂ crystallites; representative images of s-CoMo/G-IM and s-CoMo/G-HMBx are shown in Fig. 3. The black thread-like fringes are MoS₂ slabs, as confirmed by EDX. The interlayer distance between the fringes is approximately 0.62 nm, in accordance with the crystalline MoS₂ characteristic basal plane (002) [52]. The clusters of cobalt species in the catalysts are smaller than 0.5 nm, which cannot be detected by HRTEM [53]. Consequently, both the MoS₂ phases and CoMoS phases are included in the black thread-like fringes. For s-CoMo/G-IM, most of the MoS₂ slabs are multilayered and long. In contrast, most of the MoS₂ slabs on s-CoMo/G-HMBx are short and have few layers, indicating that s-CoMo/G-HMBx have superior dispersion of the active metals.

The statistical distribution results of the length and the stacking number of the MoS₂ slabs on s-CoMo/G-IM and s-CoMo/G-HMBx are presented in Fig. 4. For all of the catalysts, the MoS₂ layer number is between 1 and 7 layers and the MoS₂ slab lengths are between 2.0 and 5.0 nm. On s-CoMo/G-IM, the percentage of MoS₂ slabs with more than 3 layers exceeds 40% and the percentage of MoS₂ slabs longer than 4.0 nm exceeds 45%. With an increasing HMB content in s-CoMo/G-HMBx, the percentage of MoS₂ slabs with more than 3 layers decreases (from 20.5% of s-CoMo/G-HMB2 to 1.7% of s-CoMo/G-HMB8), and the percentage of MoS₂ slabs longer than 4 nm decreases (from 26.8% of s-CoMo/G-HMB2 to 2.1% of s-CoMo/G-HMB8). As listed in Table 2, the average layer number, the average length and the dispersion of MoS₂ slabs on s-CoMo/G-IM are 3.4, 4.2 nm and 0.26, respectively. For s-

CoMo/G-HMBx, increasing the HMB content leads to decreases in the average layer number of MoS₂ slabs (from 2.8 of s-CoMo/G-HMB2 to 1.3 of s-CoMo/G-HMB8) and the average lengths of MoS₂ slabs (from 3.7 nm of s-CoMo/G-HMB2 to 2.5 nm of s-CoMo/G-HMB8). Moreover, by increasing the HMB content in s-CoMo/G-HMBx, the MoS₂ slab dispersion increases from 0.31 for s-CoMo/G-HMB2 to 0.43 for s-CoMo/G-HMB8. The above results indicate that the morphology of MoS₂ slabs is finely adjusted through changing the content of HMB that is incorporated into s-CoMo/G-HMBx.

3.4. H₂-TPR

H₂-TPR was used to investigate the state of the active phase over the prepared catalysts, the results of which are exhibited in Fig. 5. In the H₂-TPR patterns of s-CoMo/G-IM and s-CoMo/G-HMBx, the low-temperature peak at 240 °C reflects the reduction of sulfur atoms that are weakly bonded to the catalyst surface, and the high-temperature peak at 600 °C is ascribed to the partial reduction of MoS₂ [54–56]. Compared to s-CoMo/G-IM, the temperatures of the low-temperature and high-temperature peaks of s-CoMo/G-HMBx remain unchanged, indicating that the incorporation of HMB does not change the reduction temperature of sulfur species and the reduction temperature of MoS₂ crystals; however, the areas of the low-temperature and high-temperature peaks in s-CoMo/G-HMBx increase. By increasing the HMB content in s-CoMo/G-HMBx, the area of the low-temperature peak increases. When the catalyst surface is reduced, some coordinative unsaturated sites (CUS) are produced, which are considered to be responsible for the active sites [55]. Therefore, the area of the low-temperature peak allows for the determination of the number of active sites. Therefore, s-CoMo/G-HMBx with a higher area under the low-temperature peak has a greater number of active sites than s-CoMo/G-IM, and by the increasing HMB content in s-CoMo/G-HMBx, the number of the active sites increases. The area of the high-temperature peak reflects the dispersion of active metals on the catalyst surface [57,58]. Thus, s-CoMo/G-HMBx are characterized by higher dispersion of active metals than s-CoMo/G-IM, and by increasing the HMB content in s-CoMo/G-HMBx, the dispersion of active metals increases. The minor cobalt loading on all of the catalysts results in the absence of cobalt species in the H₂-TPR patterns. The above results demonstrate that the incorporation of HMB improves the dispersion of active metals and increases the number of active sites, which is an advantage for enhancing the catalytic activity of s-CoMo/G-HMBx.

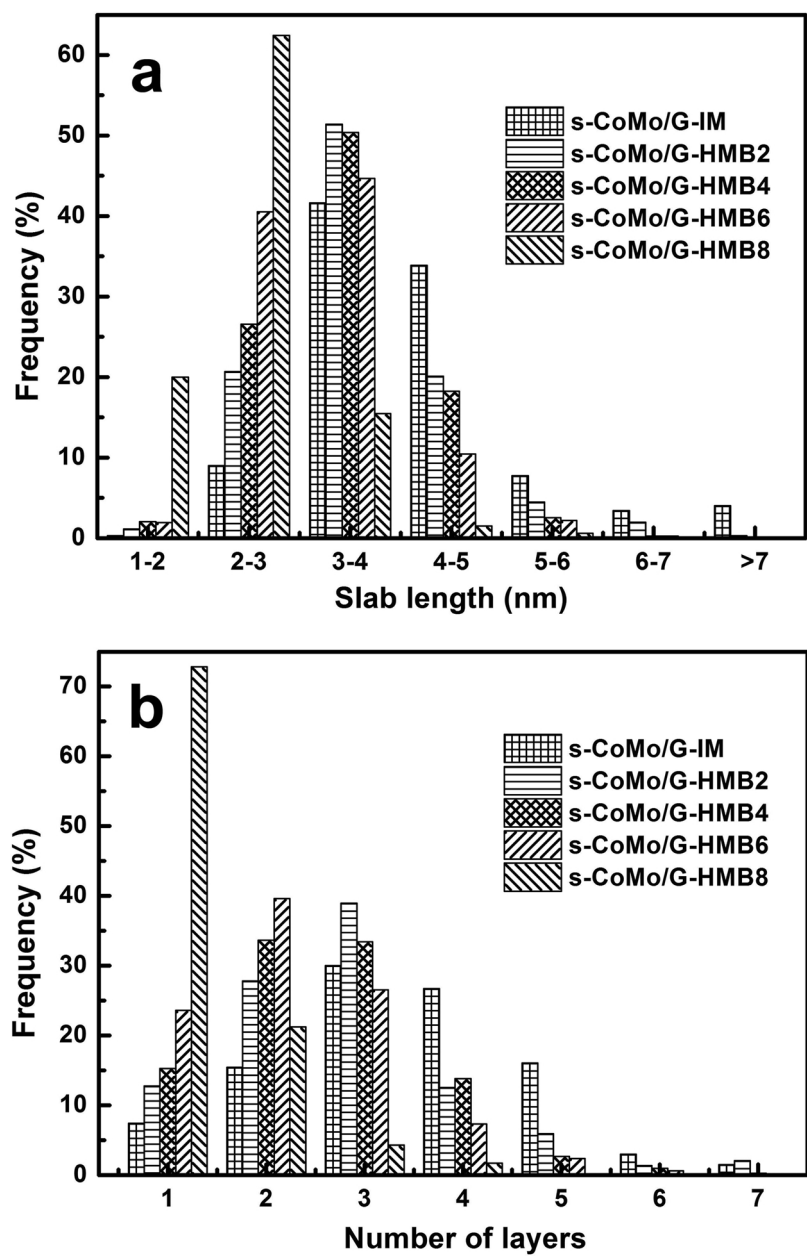


Fig. 4. Distributions of the length (a) and the layer number (b) of MoS_2 slabs on s-CoMo/G-IM and s-CoMo/G-HMBx.

Table 2
HRTEM statistics of s-CoMo/G-IM and s-CoMo/G-HMBx.

Catalyst	\bar{L} (nm)	\bar{N}	D	$\text{Mo}_{\text{sulfidation}}$
s-CoMo/G-IM	4.2	3.4	0.26	92.2
s-CoMo/G-HMB2	3.7	2.8	0.31	92.4
s-CoMo/G-HMB4	3.5	2.6	0.32	92.4
s-CoMo/G-HMB6	3.2	2.3	0.34	92.5
s-CoMo/G-HMB8	2.5	1.3	0.43	92.6

3.5. XPS

XPS experiments allow for the evaluation of the chemical state and surface composition of metal species on s-CoMo/G-IM and s-CoMo/G-HMBx. The fitted and experimental XPS spectra of Mo3d for s-CoMo/G-IM and s-CoMo/G-HMBx are shown in Fig. 6. The Mo 3d spectra were resolved into three doubles with spin-orbital splitting constants of 3.2 eV [59,60]. The binding energies of $\text{Mo3d}_{5/2}$ components are

located at 232.2 ± 0.1 eV, 230.2 ± 0.1 eV and 229.0 ± 0.1 eV, which are assigned to MoO_3 species (Mo^{6+}), MoO_xS_y oxysulfide (Mo^{5+}) and MoS_2 species (Mo^{4+}), respectively [59–61]. The peak at the binding energy of 226.0 ± 0.1 eV is assigned to sulfur species (S2s) [62]. The ratio of MoS_2 species (Mo^{4+}) to the total of MoS_2 species (Mo^{4+}), MoO_xS_y oxysulfide (Mo^{5+}) and MoO_3 species (Mo^{6+}) is defined as the sulfidation degree of Mo ($\text{Mo}_{\text{sulfidation}}$). The sulfidation degrees of s-CoMo/G-IM and s-CoMo/G-HMBx were calculated from the Mo3d XPS spectra, and the results are listed in Table 2. The sulfidation degrees of s-CoMo/G-IM and s-CoMo/G-HMBx are all greater than 92%, indicating that the Mo species are almost fully sulfidized on s-CoMo/G-IM and s-CoMo/G-HMBx. The much higher sulfidation degrees of s-CoMo/G-IM and s-CoMo/G-HMBx compared to that of commercial CoMo/Al₂O₃ result from the use of ammonium tetrathiomolybdate as the molybdenum precursor.

The experimental and fitted XPS patterns of Co2p for s-CoMo/G-IM and s-CoMo/G-HMBx are shown in Fig. 7 to determine the contents of different cobalt species. Cobalt species exist as oxidic CoO_x , sulfided

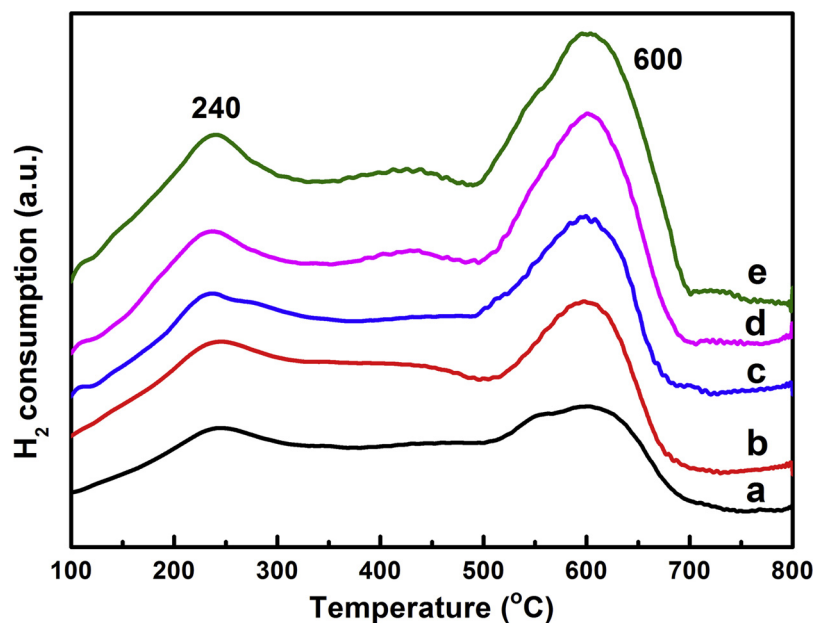


Fig. 5. H_2 -TPR patterns of s-CoMo/G-IM (a), s-CoMo/G-HMB2 (b), s-CoMo/G-HMB4 (c), s-CoMo/G-HMB6 (d) and s-CoMo/G-HMB8 (e).

CoS_x and mixed CoMoS on the surface of sulfided bimetallic CoMo catalysts. The binding energies at 797.5 ± 0.1 eV and 781.5 ± 0.1 eV are attributed to the $2\text{p}_{1/2}$ and $2\text{p}_{3/2}$ of CoO_x , and those at 793.2 ± 0.1 eV and 778.2 ± 0.1 eV are attributed to the $2\text{p}_{1/2}$ and $2\text{p}_{3/2}$ of CoS_x [41,63]. The binding energies at 778.8 ± 0.1 eV and 793.9 ± 0.1 eV are attributed to CoMoS [41]. The deconvolution results of the Co2p spectra for s-CoMo/G-IM and s-CoMo/G-HMBx are exhibited in Table 3. Among all of the catalysts, s-CoMo/G-IM has the highest percentage of CoO_x species (49.6%) and the lowest percentage of cobalt species in CoMoS (34.2%). Compared to s-CoMo/G-IM, s-CoMo/G-HMBx possess a higher percentage of CoMoS. With an increasing HMB content in s-CoMo/G-HMBx, the percentages of CoO_x (from 37.2% of s-CoMo/G-HMB2 to 28.6% of s-CoMo/G-HMB8) and CoS_x (from 15.4% of s-CoMo/G-HMB2 to 12.1% of s-CoMo/G-HMB8) species decrease gradually; the percentage of CoMoS species (from 47.4% of s-CoMo/G-HMB2 to 59.3% of s-CoMo/G-HMB8) increases gradually. Moreover, the effective cobalt content in the CoMoS phase

(C_{CoMoS}) of s-CoMo/G-HMBx is also higher than that of s-CoMo/G-IM, implying that there are more CoMoS phases on the surface of s-CoMo/G-HMBx.

3.6. Origin of the catalyst structures

The above analytical results indicate that the morphology and the content of active sites on s-CoMo/G-HMBx can be finely adjusted by changing the amount of HMB during the preparation process of the catalysts. It has been known that GO has many negative charges due to the presence of abundant oxygen-containing functional groups, such as $-\text{OH}$ and $-\text{COOH}$ [64]. The cationic $(\text{CH}_3)_3\text{N}(\text{CH}_2)_6\text{N}(\text{CH}_3)_3^{2+}$ (HMB^{2+}) can be adsorbed on the surface of the negatively charged GO via strong electrostatic interactions. To determine the electrostatic interactions between cationic HMB^{2+} and negatively charged GO, the zeta potential of HMB-functionalized GO (HMB-GO) suspension with 1 mg mL^{-1} of GO and different HMB concentrations was tested, and the

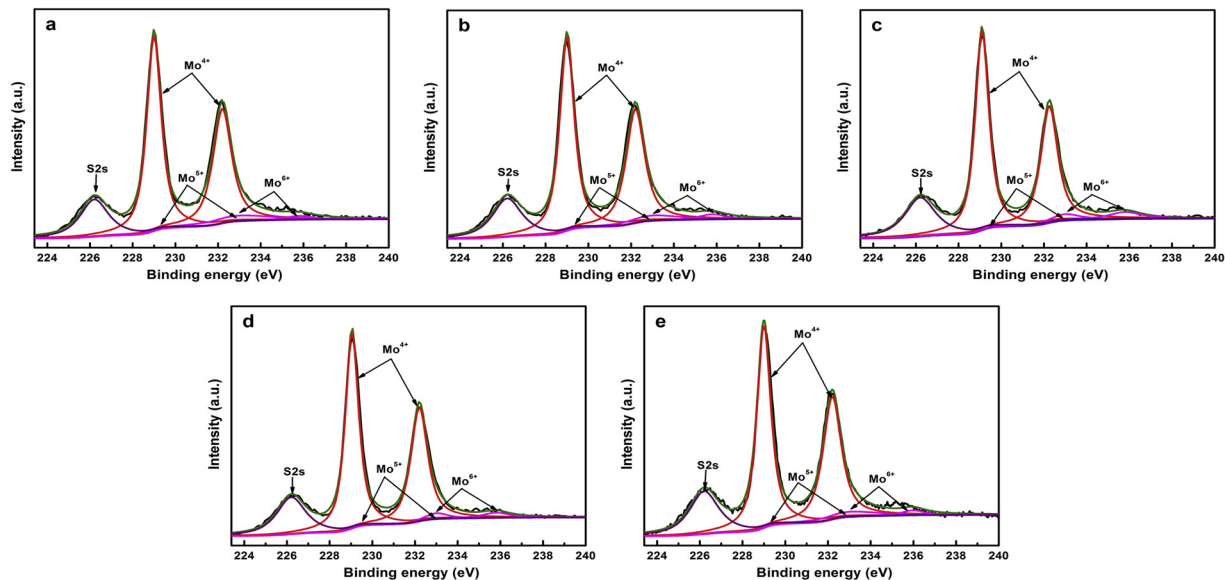


Fig. 6. Mo3d XPS patterns of s-CoMo/G-IM (a), s-CoMo/G-HMB2 (b), s-CoMo/G-HMB4 (c), s-CoMo/G-HMB6 (d) and s-CoMo/G-HMB8 (e).

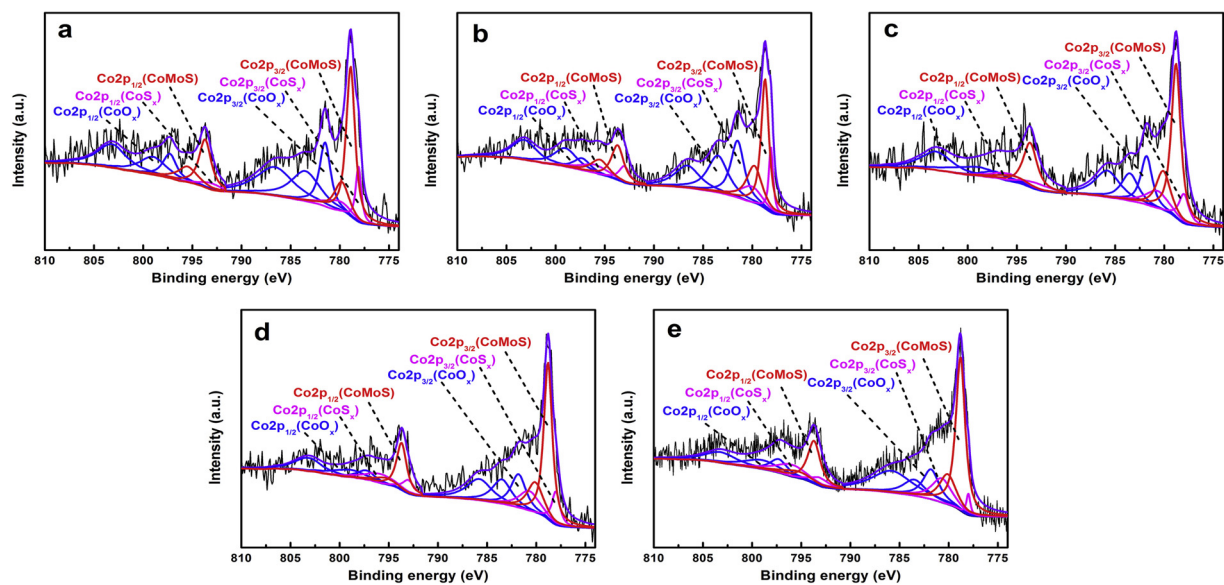


Fig. 7. Co2p XPS patterns of s-CoMo/G-IM (a), s-CoMo/G-HMB2 (b), s-CoMo/G-HMB4 (c), s-CoMo/G-HMB6 (d) and s-CoMo/G-HMB8 (e).

Table 3

Active metal content of s-CoMo/G-IM and s-CoMo/G-HMBx measured by XPS.

Catalyst	Co fraction (%)			C_{CoMoS}^a (wt.%)	C_{MoS_2} (wt.%)	$C_{\text{CoMoS}}/C_{\text{MoS}_2}$	$(f_e/f_c)_{\text{CoMo}}$ ^b
	CoO_x	CoS_x	CoMoS				
s-CoMo/G-IM	49.6	16.2	34.2	0.48	5.88	0.08	1.4
s-CoMo/G-HMB2	37.2	15.4	47.4	0.74	5.45	0.14	1.5
s-CoMo/G-HMB4	34.5	13.3	52.2	0.91	5.16	0.18	1.7
s-CoMo/G-HMB6	29.7	12.6	57.7	1.20	4.76	0.25	1.8
s-CoMo/G-HMB8	28.6	12.1	59.3	1.22	4.71	0.26	1.2

^a Effective concentration of the CoMoS phases calculated from XPS results (Eq. (6)).

^b The ratio of edge to corner Co atoms in CoMoS phases calculated from XPS and HRTEM results (Eq. (7)).

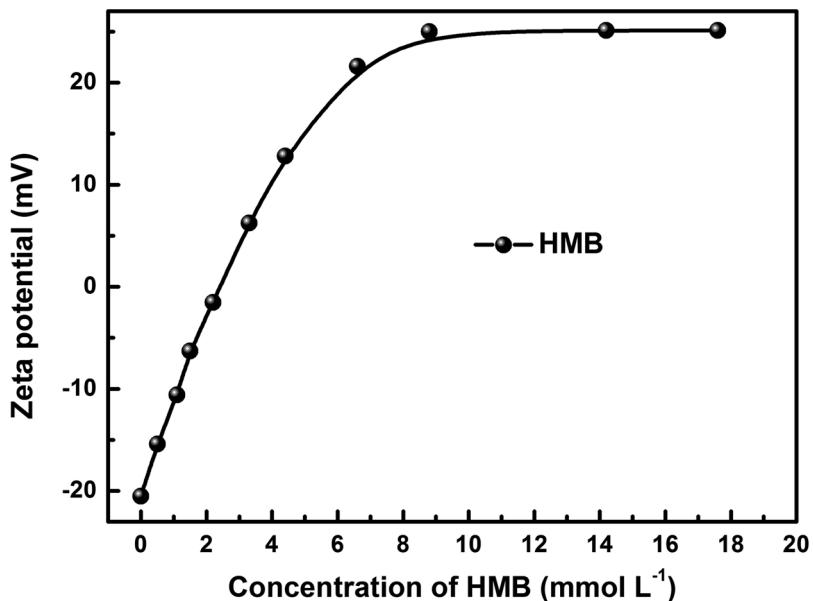


Fig. 8. Zeta potential of HMB-GO suspension with different concentrations of HMB.

results are shown in Fig. 8. For HMB-GO, with the increasing concentration of HMB, the zeta potential increases in an exponential trend. At a concentration of $\text{HMB} < 8.8 \text{ mmol L}^{-1}$, the zeta potential increases gradually from negative charges to positive charges, indicating that the HM^{2+} cations are adsorbed on the surface of GO. When the

concentration of HMB increases to 8.8 mmol L^{-1} , the zeta potential reaches its saturated value (23.4 mV). The above results indicate that the negatively charged GO can be positively charged by incorporating HMB, and with the increasing concentration of HMB, the positively charged character is enhanced until the concentration of HMB reaches

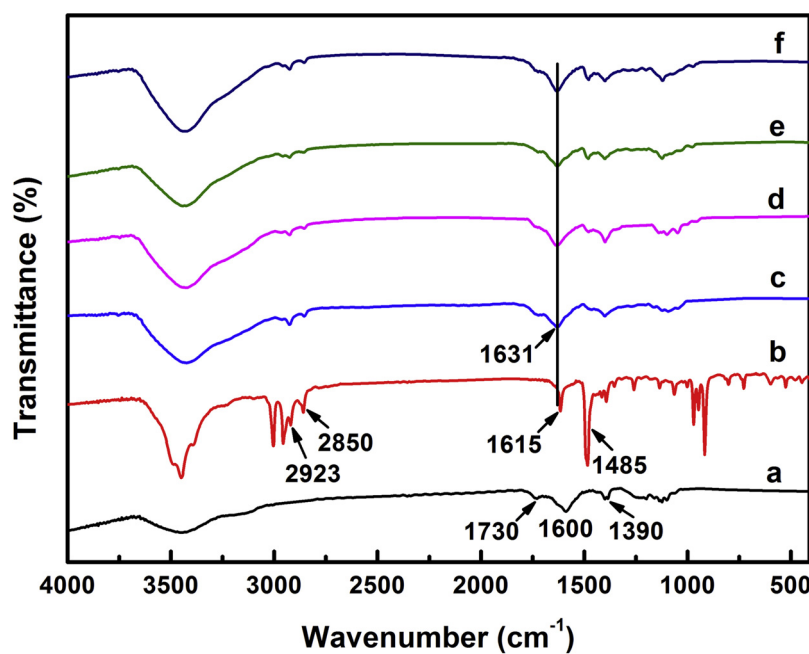


Fig. 9. FT-IR spectra of GO (a), HMB (b), HMB2-GO (c), HMB4-GO (d), HMB6-GO (e) and HMB8-GO (f).

8.8 mmol L⁻¹. After adding different amount of HM²⁺, the amount of positive charges on GO can be adjusted, which benefits to control the morphology of Mo species.

To confirm that HM²⁺ has been incorporated into GO, FT-IR experiments were performed, and the results are shown in Fig. 9. The samples show a broad peak at about 3430 cm⁻¹ that is assigned to O–H stretching vibrations of hydroxyl groups or chemisorbed water [23]. The FT-IR spectrum of GO displays three peaks at 1390, 1600 and 1730 cm⁻¹, which are ascribed to the C–OH stretching vibration, the vibration of carboxyl groups and the C=O carbonyl stretching vibration, respectively [31,65,66]. For HMB-GO, peaks appear at 1485, 2850 and 2923 cm⁻¹, attributable to the scissoring vibration of –CH₂–, the C–H stretching vibration of –CH₂– and the C–H stretching vibration of –CH₃ in HMB, respectively [50]. The original (CH₃)₃N⁺(CH₂)₆–(NR₄⁺) asymmetric bending peak of HMB (1615 cm⁻¹) was shifted to 1631 cm⁻¹ for HMB-GO, indicating that HM²⁺ interacts with the surface of GO, accompanied by a blue shift. The above results demonstrate that the carboxylic acid groups in GO are functionalized by the quaternary ammonium in HMB through electrostatic interactions.

According to the above analyses, the preparation principle of MoS₂/GO-HMBx by the HMB-assisted hydrothermal method is shown in Fig. 10. First, a suspension of HM²⁺ adsorbed GO is obtained by mixing an HMB and GO solution while stirring; the adsorption of HM²⁺ on GO converts the surface of GO into a positively charged surface, which overcomes the charge incompatibility between MoS₄²⁻ and negatively charged GO. Then, a hydrothermal process is used to prepare a MoS₄²⁻-HM²⁺-GO complex because aqueous solution under hydrothermal conditions can control the shape and size of supported Mo species due to a lower resistance to mass transfer and a decreased solution viscosity [67,68]; after the hydrothermal reaction, MoS₄²⁻ anions are uniformly adsorbed on the surface of GO through the anchoring effect of HM²⁺, and the black MoS₄²⁻-HM²⁺-GO complex is obtained. Finally, the MoS₄²⁻-HM²⁺-GO complex is calcined in N₂ and MoS₂/GO-HMBx are obtained. The remnant carbonaceous species formed by the carbonization of HMB during calcination can restrain the stacking of MoS₂ to reduce the layer number of MoS₂ slabs and the growth of MoS₂ to improve the dispersion of MoS₂ slabs [43]. The adjusted morphology of MoS₂ slabs influences the content and morphology of Co-Mo-S phases since MoS₂ can be considered as the secondary support for Co species [69]. With the increase in the HMB/Mo ratios from 2 to 8, the average

length of MoS₂ slabs decreases from 3.7 to 2.5 nm, and the average stacking numbers decreases from 2.8 to 1.3, as characterized by Raman and HRTEM. Moreover, with the increase in the HMB/Mo ratios from 2 to 8, the C_{CoMoS} value increases from 0.74 to 1.22 wt.%, as characterized by XPS.

3.7. Catalytic activity

The catalytic performances of s-CoMo/G-IM and s-CoMo/G-HMBx in the HDS of model gasoline are listed in Table 4. s-CoMo/G-IM exhibits a poor selective HDS property, with an HDS ratio of 60.6%, a *k*_{HDS} of 2.11×10^{-7} mol g⁻¹ s⁻¹, an olefin hydrogenation ratio (HYD ratio) of 10.6% and a *k*_{HYD} of 2.27×10^{-5} mol g⁻¹ s⁻¹. s-CoMo/G-HMBx have better selective HDS performance than s-CoMo/G-IM. For s-CoMo/G-HMBx, with an increasing HMB content, the HDS ratio and the *k*_{HDS} value increase (from 83.1% and 2.76×10^{-7} mol g⁻¹ s⁻¹ of s-CoMo/G-HMB2 to 94.2% and 3.72×10^{-7} mol g⁻¹ s⁻¹ of s-CoMo/G-HMB8, respectively), and the HYD ratio and the *k*_{HYD} value also increase (from 12.2% and 2.63×10^{-5} mol g⁻¹ s⁻¹ of s-CoMo/G-HMB2 to 17.9% and 3.84×10^{-5} mol g⁻¹ s⁻¹ of s-CoMo/G-HMB8, respectively). Compared to s-CoMo/G-IM, s-CoMo/G-HMBx have higher HDS activities, which result from the higher dispersion of CoMoS phases and higher content of CoMoS phases, as demonstrated by the XRD, TEM and XPS results. Compared to s-CoMo/G-IM, s-CoMo/G-HMBx exhibits a higher SF value, indicating the advantage of the latter in selective HDS. With the increasing HMB content, the SF value of s-CoMo/G-HMBx first increases and then decreases, with the optimal SF value (17.2) at s-CoMo/G-HMB6. The variation in the SF value with increasing HMB content results from variation of the content in CoMoS phases and the edge/corner ratio of CoMoS phases, as interpreted in the following section. A traditional CoMo/γ-Al₂O₃ (2.21 wt.% Co and 8.03 wt.% Mo) was also selected as a reference catalyst. The HYD ratio of the CoMo/γ-Al₂O₃ are much higher than those of s-CoMo/G-HMBx, while the HDS ratio and the SF of the CoMo/γ-Al₂O₃ is much lower than those of s-CoMo/G-HMBx (Table 4). These results indicate that graphene is a suitable support for selectivity HDS.

3.8. Interpretation for the HDS/HYD selectivity of the prepared catalysts

Miller et al. [70] reported that the olefin HYD is significantly related

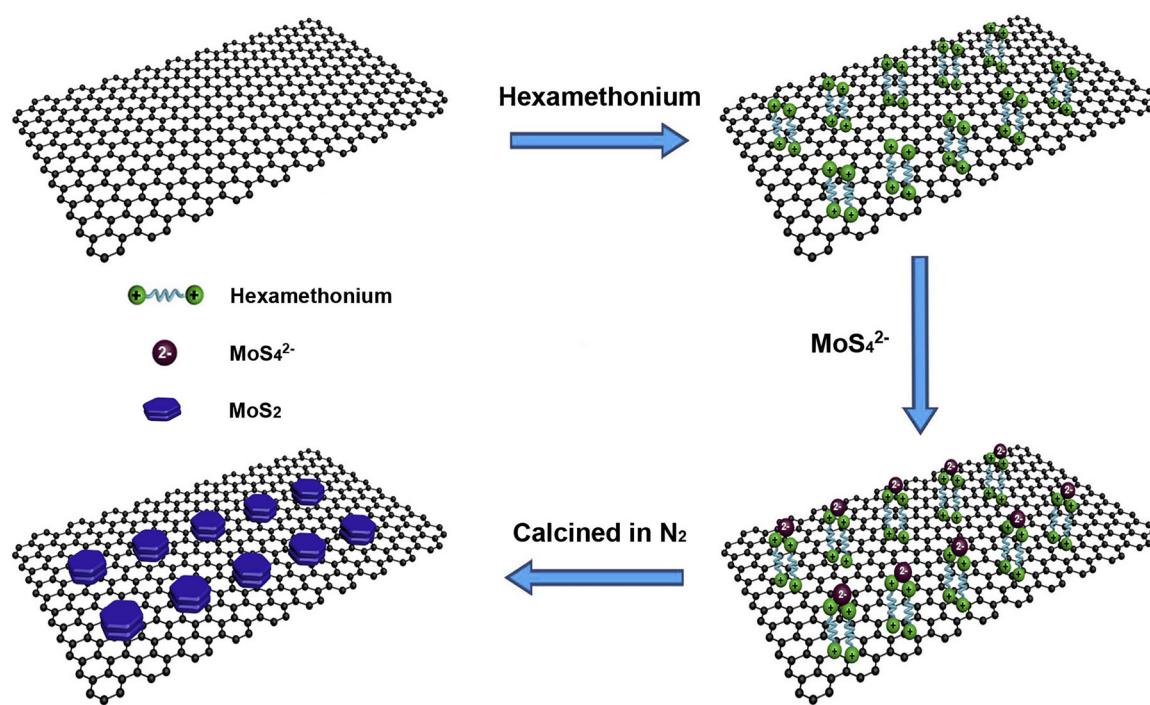


Fig. 10. Schematic diagram of the preparation principle of $\text{MoS}_2/\text{GO-HMBx}$.

to the content of unpromoted MoS_2 phases, and with the increasing content of MoS_2 , the activity of olefin saturation increases. In our previous work [7], we explored the influences of the stacking and dispersion of active phases on the HDS selectivity and found that the compromise between the stacking and dispersion of active phases is important for achieving better HDS selectivity. However, this finding does not distinguish MoS_2 and CoMoS phases. Krebs et al. [71] demonstrated that the interaction between CoMoS and thiophene is stronger than that between CoMoS and olefin, while the interaction between MoS_2 and olefin is stronger than that between MoS_2 and thiophene. Therefore, the further investigation about the influences of MoS_2 and CoMoS phases on the HDS and the olefin hydrogenation are necessary, to which this work is addressed. According to Table 4, the SF value of $s\text{-CoMo/G-IM}$ is lower than $s\text{-CoMo/G-HMBx}$, which results from the much lower $C_{\text{CoMoS}}/C_{\text{MoS}_2}$ ratio in $s\text{-CoMo/G-IM}$ compared to that in $s\text{-CoMo/G-HMBx}$. For $s\text{-CoMo/G-HMBx}$, when the HMB/Mo ratio is less than 6.0, with increasing HMB content, the $C_{\text{CoMoS}}/C_{\text{MoS}_2}$ ratio increases from 0.14 of $s\text{-CoMo/G-HMB2}$ to 0.25 of $s\text{-CoMo/G-HMB6}$, resulting in an increase in the SF value; when the HMB/Mo ratio exceeds 6.0, $s\text{-CoMo/G-HMB6}$ and $s\text{-CoMo/G-HMB8}$ have almost the same $C_{\text{CoMoS}}/C_{\text{MoS}_2}$ ratio, but their SF values are very different. It has been reported that the corner sites on the CoMoS phases are favorable for HYD reactions and edge sites on the CoMoS phases promote HDS

reactions because the corner sites are favored more for the adsorption and dissociation of molecular hydrogen into ionic hydrogen. Nikulshin et al. [19] proposed that the HDS/HYD selectivity is linearly correlative with the ratio of edge to corner Co atoms in CoMoS (f_e/f_c)_{CoMo}, and increasing the content of edge Co atoms while decreasing the content of corner Co atoms in CoMoS improves the HDS/HYD selectivity. Thus, $s\text{-CoMo/G-HMB6}$ with 1.8 of the $(f_e/f_c)_{\text{CoMo}}$ value has more edge Co atoms in CoMoS than $s\text{-CoMo/G-HMB8}$ with 1.2 of the $(f_e/f_c)_{\text{CoMo}}$ value (Table 3), which enhances the HDS/HYD selectivity of the former. This investigation enriches and deepens the understanding about the correlation between the morphology of active phases and the HDS selectivity.

4. Conclusions

This investigation proposes a strategy for preparing CoMoS active phases with finely tuned morphologies on graphene via the hexamethonium-assisted hydrothermal method. In this method, the negatively charged surface of GO is converted into a positively charged surface by anchoring hexamethonium cations through an electrostatic interaction, which overcomes the charge incompatibility between MoS_4^{2-} and negatively charged GO. As a result, the MoS_2 slabs are highly dispersed on GO. The morphologies of CoMoS active phases are tuned by changing

Table 4
HDS and HYD activities of $s\text{-CoMo/G-IM}$ and $s\text{-CoMo/G-HMBx}$.

Catalyst	HYD ratio ^a (%)	k_{HYD} ^b ($10^{-5} \text{ mol g}^{-1} \text{ s}^{-1}$)	HDS ratio ^a (%)	k_{HDS} ^c ($10^{-7} \text{ mol g}^{-1} \text{ s}^{-1}$)	SF
$s\text{-CoMo/G-IM}$	10.6	2.27	60.6	2.11	8.3
$s\text{-CoMo/G-HMB2}$	12.2	2.63	83.1	2.76	13.6
$s\text{-CoMo/G-HMB4}$	13.5	2.80	90.0	3.09	15.8
$s\text{-CoMo/G-HMB6}$	14.3	3.15	93.0	3.43	17.2
$s\text{-CoMo/G-HMB8}$	17.9	3.84	94.2	3.72	14.5
$\text{CoMo}/\gamma\text{-Al}_2\text{O}_3$	32.3	8.92	75.2	2.43	3.6

^a the HYD ratios of 1-hexene and the HDS ratios of thiophene on the different catalysts assessed with the conditions: $\text{H}_2/\text{model gasoline} = 300 (\text{v/v})$, $P = 1.5 \text{ MPa}$, $T = 280^\circ \text{C}$ and liquid hourly space velocity (LHSV) = 4 h^{-1} .

^b Calculated with the 1-hexene conversion at about 10%.

^c Calculated with the thiophene conversion at about 10%.

the added content of HMB. With the HMB/Mo ratio at 6.0, the catalyst presents the highest HDS selectivity among all the catalysts because it possesses the highest ratio of edge to corner Co atoms in CoMoS with a superior CoMoS/MoS₂ ratio. By adjusting the HMB/Mo ratio to finely tune the morphology of CoMoS active phases, a highly selective HDS catalyst using graphene as support is created.

Acknowledgments

The authors gratefully acknowledge the financial support of the National Natural Science Foundation of China (Grant Nos. 21076228 and U1162116).

Appendix A. Supplementary data

Supplementary material related to this article can be found, in the online version, at doi:<https://doi.org/10.1016/j.apcatb.2018.11.065>.

References

- [1] B. Liu, Y. Chai, Y. Li, A. Wang, Y. Liu, C. Liu, *Fuel* 123 (2014) 43–51.
- [2] T. Huang, Q. Peng, W. Shi, J. Xu, Y. Fan, *Appl. Catal. B-Environ.* 230 (2018) 154–164.
- [3] T.A. Saleh, K.O. Sulaiman, S.A. Al-Hammedi, H. Dafalla, G.I. Danmaliki, *J. Clean. Prod.* 154 (2017) 401–412.
- [4] T. Kaufmann, A. Kaldor, G. Stuntz, M. Kerby, L. Ansell, *Catal. Today* 62 (2000) 77–90.
- [5] S. Brunet, D. Mey, G. Péro, C. Bouchy, F. Diehl, *Appl. Catal. A-Gen.* 278 (2005) 143–172.
- [6] M. Toba, Y. Miki, Y. Kanda, T. Matsui, M. Harada, Y. Yoshimura, *Catal. Today* 104 (2005) 64–69.
- [7] Y. Fan, G. Shi, H. Liu, X. Bao, *Appl. Catal. B-Environ.* 91 (2009) 73–82.
- [8] S.A. Al-Hammedi, A.M. Al-Amer, T.A. Saleh, *Chem. Eng. J.* 345 (2018) 242–251.
- [9] C. Song, *Catal. Today* 86 (2003) 211–263.
- [10] J. Xu, T. Huang, Y. Fan, *Appl. Catal. B-Environ.* 203 (2017) 839–850.
- [11] H. Ge, X.-D. Wen, M.A. Ramos, R.R. Chianelli, S. Wang, J. Wang, Z. Qin, Z. Lyu, X. Li, *ACS Catal.* 4 (2014) 2556–2565.
- [12] X. Wang, Z. Zhao, P. Zheng, Z. Chen, A. Duan, C. Xu, J. Jiao, H. Zhang, Z. Cao, B. Ge, *J. Catal.* 344 (2016) 680–691.
- [13] S. Hatanaka, M. Yamada, O. Sadakane, *Ind. Eng. Chem. Res.* 36 (1997) 5110–5117.
- [14] D. Ishutenko, P. Minaev, Y. Anashkin, M. Nikulshina, A. Mozhaev, K. Maslakov, P. Nikulshin, *Appl. Catal. B-Environ.* 203 (2017) 237–246.
- [15] B. Baubet, M. Girleanu, A.-S. Gay, A.-L. Taleb, M. Moreraud, F. Wahl, V. Delattre, E. Devers, A. Hugon, O. Ersen, P. Afanasyev, P. Raybaud, *ACS Catal.* 6 (2016) 1081–1092.
- [16] Y. Fan, J. Lu, G. Shi, H. Liu, X. Bao, *Catal. Today* 125 (2007) 220–228.
- [17] D.I. Ishutenko, P.A. Nikul'shin, V.V. Konovalov, A.A. Pimerzin, *Kinet. Catal.* 56 (2015) 747–757.
- [18] E. Hensen, P. Kooyman, Y. Van der Meer, A. Van der Kraan, V. De Beer, J. Van Veen, R. Van Santen, *J. Catal.* 199 (2001) 224–235.
- [19] P.A. Nikulshin, D.I. Ishutenko, A.A. Mozhaev, K.I. Maslakov, A.A. Pimerzin, *J. Catal.* 312 (2014) 152–169.
- [20] M. Li, H. Li, F. Jiang, Y. Chu, H. Nie, *Catal. Today* 149 (2010) 35–39.
- [21] D. Ishutenko, P. Nikulshin, A. Pimerzin, *Catal. Today* 271 (2016) 16–27.
- [22] D. Ishutenko, P. Nikulshin, A. Pimerzin, *Catal. Today* (2016).
- [23] G.I. Danmaliki, T.A. Saleh, *J. Clean. Prod.* 117 (2016) 50–55.
- [24] G.I. Danmaliki, T.A. Saleh, *Chem. Eng. J.* 307 (2017) 914–927.
- [25] J.C. Duchet, E.M. van Oers, V.H.J. de Beer, R. Prins, *J. Catal.* 80 (1983) 386–402.
- [26] G.M.K. Abotsi, A.W. Scaroni, *Fuel Process. Technol.* 22 (1989) 107–133.
- [27] M.A. Al-Daous, *Catal. Commun.* 72 (2015) 180–184.
- [28] Z. Hajjar, M. Kazemeini, A. Rashidi, M. Bazmi, *Fuel* 165 (2016) 468–476.
- [29] H. Wang, B. Xiao, X. Cheng, C. Wang, L. Zhao, Y. Zhu, J. Zhu, X. Lu, *Appl. Catal. A-Gen.* 502 (2015) 157–165.
- [30] J. Kim, L.J. Cote, F. Kim, W. Yuan, K.R. Shull, J. Huang, *J. Am. Chem. Soc.* 132 (2010) 8180–8186.
- [31] C. Song, D. Wu, F. Zhang, P. Liu, Q. Lu, X. Feng, *Chem. Commun.* 48 (2012) 2119–2121.
- [32] P.V. Kamat, *J. Phys. Chem. Lett.* 2 (2011) 242–251.
- [33] N. Li, G. Liu, C. Zhen, F. Li, L. Zhang, H.-M. Cheng, *Adv. Funct. Mater.* 21 (2011) 1717–1722.
- [34] V. Chabot, D. Higgins, A. Yu, X. Xiao, Z. Chen, J. Zhang, *Energy Environ. Sci.* 7 (2014) 1564–1596.
- [35] F. Zhang, H. Jiang, X. Li, X. Wu, H. Li, *ACS Catal.* 4 (2014) 394–401.
- [36] W. Zhou, M. Liu, Q. Zhang, Q. Wei, S. Ding, Y. Zhou, *ACS Catal.* (2017) 7665–7679.
- [37] Y. Gao, W. Han, X. Long, H. Nie, D. Li, *Appl. Catal. B-Environ.* 224 (2018) 330–340.
- [38] S. Kasztelan, H. Toulhoat, J. Grimblot, J.P. Bonnelle, *Appl. Catal.* 13 (1984) 127–159.
- [39] T. Huang, J. Xu, Y. Fan, *Appl. Catal. B-Environ.* 220 (2018) 42–56.
- [40] A.D. Gandubert, E. Krebs, C. Legens, D. Costa, D. Guillaume, P. Raybaud, *Catal. Today* 130 (2008) 149–159.
- [41] A. Gandubert, C. Legens, D. Guillaume, S. Rebours, E. Payen, *Oil Gas Sci. Technol.* 62 (2007) 79–89.
- [42] P. Nikulshin, D. Ishutenko, Y. Anashkin, A. Mozhaev, A. Pimerzin, *Fuel* 182 (2016) 632–639.
- [43] L. Yang, X.-Z. Wang, Y. Liu, Z.-F. Yu, J.-J. Liang, B.-B. Chen, C. Shi, S. Tian, X. Li, J.-S. Qiu, *Appl. Catal. B-Environ.* 200 (2017) 211–221.
- [44] Y.-C. Chiang, P.-C. Chiang, C.-P. Huang, *Carbon* 39 (2001) 523–534.
- [45] K.S.W. Sing, R.T. Williams, *Adsorpt. Sci. Technol.* 22 (2004) 773–782.
- [46] P.A. Nikulshin, A.V. Mozhaev, A.A. Pimerzin, V.V. Konovalov, A.A. Pimerzin, *Fuel* 100 (2012) 24–33.
- [47] X. Zhang, X.-F. Qiao, W. Shi, J.-B. Wu, D.-S. Jiang, P.-H. Tan, *Chem. Soc. Rev.* 44 (2015) 2757–2785.
- [48] C. Lee, H. Yan, L.E. Brus, T.F. Heinz, J. Hone, S. Ryu, *ACS Nano* 4 (2010) 2695–2700.
- [49] L. Hong, Z. Qing, Y.C.C. Ray, T.B. Kang, E.T.H. Tong, O. Aurelien, B. Dominique, *Adv. Funct. Mater.* 22 (2012) 1385–1390.
- [50] G. Huang, T. Chen, W. Chen, Z. Wang, K. Chang, L. Ma, F. Huang, D. Chen, J.Y. Lee, *Small* 9 (2013) 3693–3703.
- [51] Z. Wang, T. Chen, W. Chen, K. Chang, L. Ma, G. Huang, D. Chen, J.Y. Lee, *J. Mater. Chem. A* 1 (2013) 2202–2210.
- [52] E. Payen, R. Hubaut, S. Kasztelan, O. Poulet, J. Grimblot, *J. Catal.* 147 (1994) 123–132.
- [53] S. Eijlsbouts, L.C.A. van den Oetelaar, R.R. van Puijenbroek, *J. Catal.* 229 (2005) 352–364.
- [54] C.J.H. Jacobsen, E. Törnqvist, H. Topsøe, *Catal. Lett.* 63 (1999) 179–183.
- [55] P. Afanasyev, *Appl. Catal. A-Gen.* 303 (2006) 110–115.
- [56] B. Yoosuk, J.H. Kim, C. Song, C. Ngamcharussrivichai, P. Prasassarakich, *Catal. Today* 130 (2008) 14–23.
- [57] B. Liu, Y. Chai, Y. Li, A. Wang, Y. Liu, C. Liu, *Appl. Catal. A-Gen.* 471 (2014) 70–79.
- [58] P. Li, X. Liu, C. Zhang, Y. Chen, B. Huang, T. Liu, Z. Jiang, C. Li, *Appl. Catal. A-Gen.* 524 (2016) 66–76.
- [59] T.K.T. Ninh, D. Laurenti, E. Leclerc, M. Vrinat, *Appl. Catal. A-Gen.* 487 (2014) 210–218.
- [60] T.K.T. Ninh, L. Massin, D. Laurenti, M. Vrinat, *Appl. Catal. A-Gen.* 407 (2011) 29–39.
- [61] K.A. Nadeina, O.V. Klimov, I.G. Danilova, V.Y. Pereyma, E.Y. Gerasimov, I.P. Prosvirin, A.S. Noskov, *Appl. Catal. B-Environ.* 223 (2018) 22–35.
- [62] D. Laurenti, B. Phung-Ngoc, C. Roukoss, E. Devers, K. Marchand, L. Massin, L. Lemaitre, C. Legens, A.-A. Quoineaud, M. Vrinat, *J. Catal.* 297 (2013) 165–175.
- [63] L. van Haandel, G.M. Bremmer, E.J.M. Hensen, T. Weber, *J. Catal.* 342 (2016) 27–39.
- [64] K. Zhang, L. Mao, L.L. Zhang, H.S. On Chan, X.S. Zhao, J. Wu, *J. Mater. Chem.* 21 (2011) 7302–7307.
- [65] Y. Liang, D. Wu, X. Feng, M. Klaus, *Adv. Mater.* 21 (2009) 1679–1683.
- [66] Y. Si, E.T. Samulski, *Nano Lett.* 8 (2008) 1679–1682.
- [67] M. Kang, S.-J. Choung, J.Y. Park, *Catal. Today* 87 (2003) 87–97.
- [68] Y. Fan, H. Xiao, G. Shi, H. Liu, X. Bao, *Energy Environ. Sci.* 4 (2011) 572–582.
- [69] Y. Okamoto, K. Ochiai, M. Kawano, T. Kubota, *J. Catal.* 222 (2004) 143–151.
- [70] J.T. Miller, W.J. Reagan, J.A. Kaduk, C.L. Marshall, A.J. Kropf, *J. Catal.* 193 (2000) 123–131.
- [71] E. Krebs, B. Silvi, A. Daudin, P. Raybaud, *J. Catal.* 260 (2008) 276–287.